

Dynamics of van der Waals Charge Qubit in 2D Bilayers: *Ab initio* Quantum Transport and Qubit Measurement

Jiang Cao,¹ Guido Gandus,^{1,2} Tarun Agarwal,³ Mathieu Luisier,¹ and Youseung Lee^{1,*}

¹*Integrated Systems Laboratory, ETH Zürich, 8092 Zürich, Switzerland*

²*Empa, Swiss Federal Laboratories for Materials Science and Technology, Überlandstrasse 129, 8600 Dübendorf, Switzerland*

³*Department of Electrical Engineering, IIT Gandhinagar, Gandhinagar, India*

A van der Waals (vdW) charge qubit, electrostatically confined within two-dimensional (2D) vdW materials, is proposed as building block of future quantum computers. Its characteristics are systematically evaluated with respect to its two-level anti-crossing energy difference (Δ). Bilayer graphene ($\Delta \approx 0$) and a vdW heterostructure ($\Delta \gg 0$) are used as representative examples. Their tunable electronic properties with an external electric field define the state of the charge qubit. By combining density functional theory and quantum transport calculations, we highlight the optimal qubit operation conditions based on charge stability and energy-level diagrams. Moreover, a single-electron transistor (SET) design based on trilayer vdW heterostructures capacitively coupled to the charge qubit is introduced as measurement setup with low decoherence and improved measurement properties. It is found that a Δ greater than 20 meV results in a rapid mixing of the qubit states, which leads to a lower measurement quantity, i.e. contrast and conductance. With properly optimized designs, qubit architectures relying on 2D vdW structures could be integrated into an all-electronic quantum computing platform.

I. INTRODUCTION

Emerging nanoelectronic devices are widely seen as key enablers of future quantum computers that will be able to solve intractable problems for classical machines. A wide range of qubit platforms have already been experimentally demonstrated, e.g. charge, spin, superconducting, and trapped-ion qubits [1–4]. In all these approaches, a large number of physical qubits are required to realize one single logical qubit [5]. The ideal qubit structure should therefore be scalable and integrable with the existing CMOS technology to build a large-scale quantum computer.

Quantum dots (QD) offer a great platform to generate CMOS-compatible qubits based on the spin and/or electronic orbital degrees of freedom of electrons [6–8]. For example, silicon spin qubits show very long coherence times up to milliseconds at low temperature [2]. However, they are rather challenging to handle due to the rapid flip-flop of single electron spins. Charge qubits, on the other hand, can simplify the read-out of qubits thanks to well-developed technologies such as single-electron transistors (SET). Moreover, these qubits can be directly operated by electrodes up to gigahertz rates.

Two-dimensional (2D) materials represent a promising alternative to conventional semiconductors to host qubits owing to the wide tunability of their electronic properties and the manifold quantum phenomena that emerge in the atomically thin limit such as massless Dirac fermions [9], anyons [10], or the quantum spin Hall effect [11]. In addition, the van der Waals (vdW) stacking of 2D materials provides versatility in growth, functional-

ization, and heterostructure integration, which facilitates the processing of complex systems. AB-stacked bilayer graphene (BLG), a vdW homojunction, is an excellent example: its band gap can be gradually modified by applying an external electric field [12–18]. Moreover, the electric field can modify the quantum superposition of wave functions localized in different layers, affecting both the conduction and valence bands of BLG. The same effect can be obtained in other vdW structures as well if the band edges of the individual 2D materials that constitute the stack get nearly aligned on an absolute energy scale [19]. Based on this observation, vdW structures are attractive to implement charge qubits capable of switching between two states with the help of a vertical electric field [20]. However, for vdW charge qubits to become a viable option, an all-electronic platform that can host multiple QDs should be available. The coupling between neighboring QDs should be tunable, while it should be possible to measure the qubit state with low decoherence.

In this work, we propose a platform for vdW charge qubits that takes advantage of quantum superposition of the top and bottom charge states formed by vdW bilayers, as illustrated in Fig. 1(a), and we analyze its potential through *ab initio* device simulations. Differently from the conventional charge qubits that require two QDs, e.g. the left and right QDs, a single QD of bilayer acts as an individual qubit. As a promising candidate, we showcase the functionality of a BLG vdW charge qubit system. The role of two-level anti-crossing energies Δ is analyzed for two exemplary vdW materials that illustrate the extreme cases of Δ : BLG ($\Delta \approx 0$) and $\text{ZrS}_2\text{-HfS}_2$ ($\Delta = 0.174$ eV). As a first step, density functional theory (DFT) and quantum transport calculations are combined to study the charge stability diagram and energy-level spectrum of multiple vdW charge qubits with tunable coupling, formed on an electrostatically confined BLG

* Corresponding author: youseung.lee@iis.ee.ethz.ch

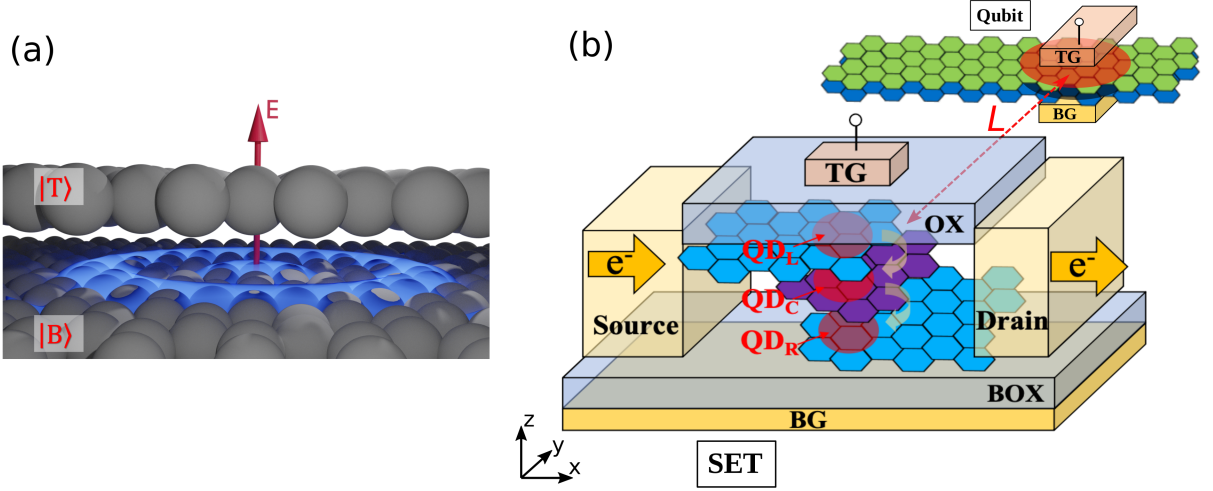


FIG. 1. (a) Sketch of a charge qubit system implemented on a 2D bilayer material to which a vertical electric field \vec{E} is applied. The wave functions localized in the bottom and top layers are labeled $|B\rangle$ and $|T\rangle$, respectively. (b) Schematic of the proposed qubit measurement setup where three QDs labeled $QD_{L,C,R}$ are confined inside a vdW trilayer $MoS_2-WSe_2-MoS_2$ heterostructure controlled by a top (TG) and bottom gate (BG) and connected to a source and drain contact forming altogether a single-electron transistor (SET). The trilayer $MoS_2-WSe_2-MoS_2$ SET is electrostatically coupled to the charge qubit located on the BLG. The distance between the SET and qubit is L .

device. It should be pointed out that directly coupled read-out leads, as originally proposed in the paper of Luccatto *et al.* [20], can be prominent sources of decoherence due to the finite tunnel coupling of the reservoirs to the charge qubit. As a consequence, it might be experimentally difficult to measure the qubit state. To overcome this issue, we designed a novel measurement setup using triple-QD SETs based on a trilayer vdW heterostructure electrostatically coupled to our vdW charge qubits, as depicted in Fig. 1(b). Here, its influence will be simulated through the Lindblad master equation with the QuTiP package [21] using a phenomenological model including the important physics of decoherence. Our results highlight that 2D vdW structures can provide highly integrable all-electronic universal qubits. Moreover, our findings indicate that devices with $\Delta \gg 20$ meV pose specific design challenges related to the material combination and geometrical parameters. Hence, a careful selection of the Δ value is necessary to design properly working vdW charge qubits.

II. VDW CHARGE QUBIT MANIPULATION

We first examine the effect of a vertical electric field on the selected 2D vdW bilayer materials, BLG and ZrS_2-HfS_2 , and show that the electric-field externally applied to the bilayers can be used to control the wave function localized in the top or bottom layer to construct the qubit states. The BLG band structure without and with electric field is shown in Figs. 2(a) and 2(b), respectively. The detailed DFT simulation procedure that was used to compute those quantities can be found in Appendix A. The conduction band minimum (CBM) and

valence band maximum (VBM) are chosen as the two-level qubit states ($|0\rangle$ and $|1\rangle$) in the case of BLG, while the first and second lowest conduction bands of the ZrS_2-HfS_2 heterostructure play the same role. One importance for vdW bilayers to properly act as qubits is the existence of two bands lying quite close to each other and that can be easily inverted by applying a practical electric field.

In the BLG system without electric field \vec{E} , the $|0\rangle$ and $|1\rangle$ states are made of exactly equal contributions from each graphene layer due to the inversion symmetry of this material. A bandgap can be opened by applying a symmetry-breaking vertical \vec{E} . The vdW charge qubit states, $|0\rangle$ and $|1\rangle$, are constructed by combining the wave functions localized in the top and bottom layers, $|T\rangle$ and $|B\rangle$, respectively.

By applying a positive \vec{E} along the $+z$ direction, as in Fig. 1(a), the bands of the bottom graphene layer are lowered in energy, which increases the $|B\rangle$ character of $|0\rangle$, while $|1\rangle$ becomes more localized in the top graphene layer. The opposite behavior happens with \vec{E} pointing along the $-z$ direction. The contribution of each layer to the Bloch wave function of $|0\rangle$ and $|1\rangle$ strongly depends on the vertical electric field. An electron wave function $|\psi(\vec{E})\rangle$ can be written as the superposition of the wave functions $|T\rangle$ and $|B\rangle$ for a given \vec{E}

$$|\psi(\vec{E})\rangle = t_\psi(\vec{E}) |T\rangle + b_\psi(\vec{E}) |B\rangle, \quad (1)$$

where $t_\psi(\vec{E})$ and $b_\psi(\vec{E})$ are complex coefficients depending on \vec{E} . Due to the vdW gap between the two layers, the $|T\rangle$ and $|B\rangle$ states have a relatively small overlap and form a quasi-orthogonal basis. The $t_\psi(\vec{E})$ and

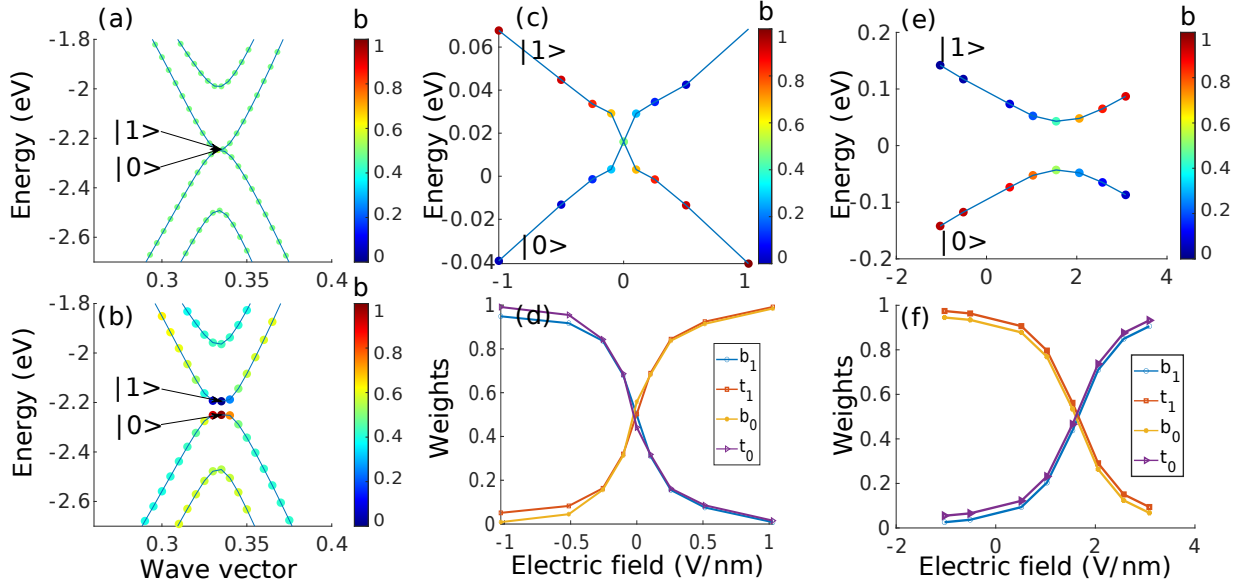


FIG. 2. Electronic bandstructure of BLG (a) without and (b) with an electric field of 0.5 V/nm. The color of the different states indicates the $|b_{0,1}|^2$ weights, which result from the projection of the atomic wave functions onto the bottom graphene layer. The valence band maximum and conduction band minimum define the $|0\rangle$ and $|1\rangle$ states. (c) Energy-level vs. electric field for the $|0\rangle$ and $|1\rangle$ states in BLG. (d) Corresponding $|b_{0,1}|^2$ and $|t_{0,1}|^2$ weights vs. electric field. (e) Same as (c) but for ZrS₂-HfS₂. (f) Same as (d) but for ZrS₂-HfS₂.

$b_\psi(\vec{E})$ coefficients satisfy the normalization condition $|t_\psi|^2 + |b_\psi|^2 = 1$.

Figure 2(c) shows the energy level of the $|0\rangle$ and $|1\rangle$ states and the $|B\rangle$ contribution to them as a function of \vec{E} . In Fig. 2(d) the $|t_{0,1}|^2$ and $|b_{0,1}|^2$ weights of the $|0\rangle$ and $|1\rangle$ states are plotted, highlighting a complementary relation between them. Here, we note that by tuning \vec{E} we can readily address any coherent superposition of the basic quantum states $|B\rangle$ and $|T\rangle$. The state $|\psi\rangle$ can be equivalently described by a Bloch vector in the standard Bloch sphere representation, where the coefficients are given by a polar θ and azimuthal angle ϕ such that $t_\psi = \cos(\theta/2)$ and $b_\psi = \sin(\theta/2)e^{i\phi}$. Moreover, under a reasonably strong positive/negative electric field, the $|0\rangle$ and $|1\rangle$ states can be localized in either the top or bottom layer, thus enabling the “must-have” qubit initialization process.

A similar behavior is observed for the first and second lowest conduction band states of ZrS₂-HfS₂, as depicted in Fig. 2(e) and (f). Due to the energy offset in the natural band alignment of the vdW heterostructure, a non-zero \vec{E}_{ac} is required to reach the crossing point where the layer contributions are equal. At this point, a so-called anti-crossing energy Δ can be introduced. The latter is then a material parameter and determined as the difference between the energies of the $|1\rangle$ and $|0\rangle$ eigenstates [1]. Table I summarizes the values of Δ for the considered vdW structures. For BLG, we note that $\Delta \gtrsim 20 \mu\text{eV}$ was observed in previous experiments [14, 22, 23] due to the presence of symmetry-breaking factors even in the absence of an electric field,

for example spin-orbit coupling, surrounding substrate atoms, or local strain.

By comparing our results to the ZrSe₂-SnSe₂ vdW heterostructure investigated in the original paper of Lucatto *et al.* [20], we notice that the Bloch vector of the BLG and ZrS₂-HfS₂ systems covers a larger θ interval for electric fields within ± 3 V/nm. For BLG, the full range of θ can be achieved with a small electric field of less than 1 V/nm, thus making BLG the most technologically appealing candidate.

A quantum control technique over the angle ϕ (*i.e.* relative phase of the wave functions) applicable to the vdW charge qubits has been proposed in Ref. 24. It relies on the Landau-Zener-Stückelberg (LZS) interference when the system non-adiabatically sweeps through the intersection point. Based on this technique, general rotations in the Bloch sphere and universal single qubit operations have already been experimentally demonstrated for Si and GaAs DQD charge qubits [1, 24].

III. QUANTUM TRANSPORT SIMULATIONS

To create a clear two-level system with a $|0\rangle$ and $|1\rangle$ state, the QDs in the vdW bilayers must be formed electrically through gate electrodes that induce a local confinement, as illustrated in Fig. 3(a). In the proposed device setup, a bottom gate uniformly acts on the BLG encapsulated within two hBN dielectric layers to electrostatically control the Fermi level. A transport channel can be defined through the BLG. Separated by an oxide, three top gates labeled L, M, and R are placed. By ap-

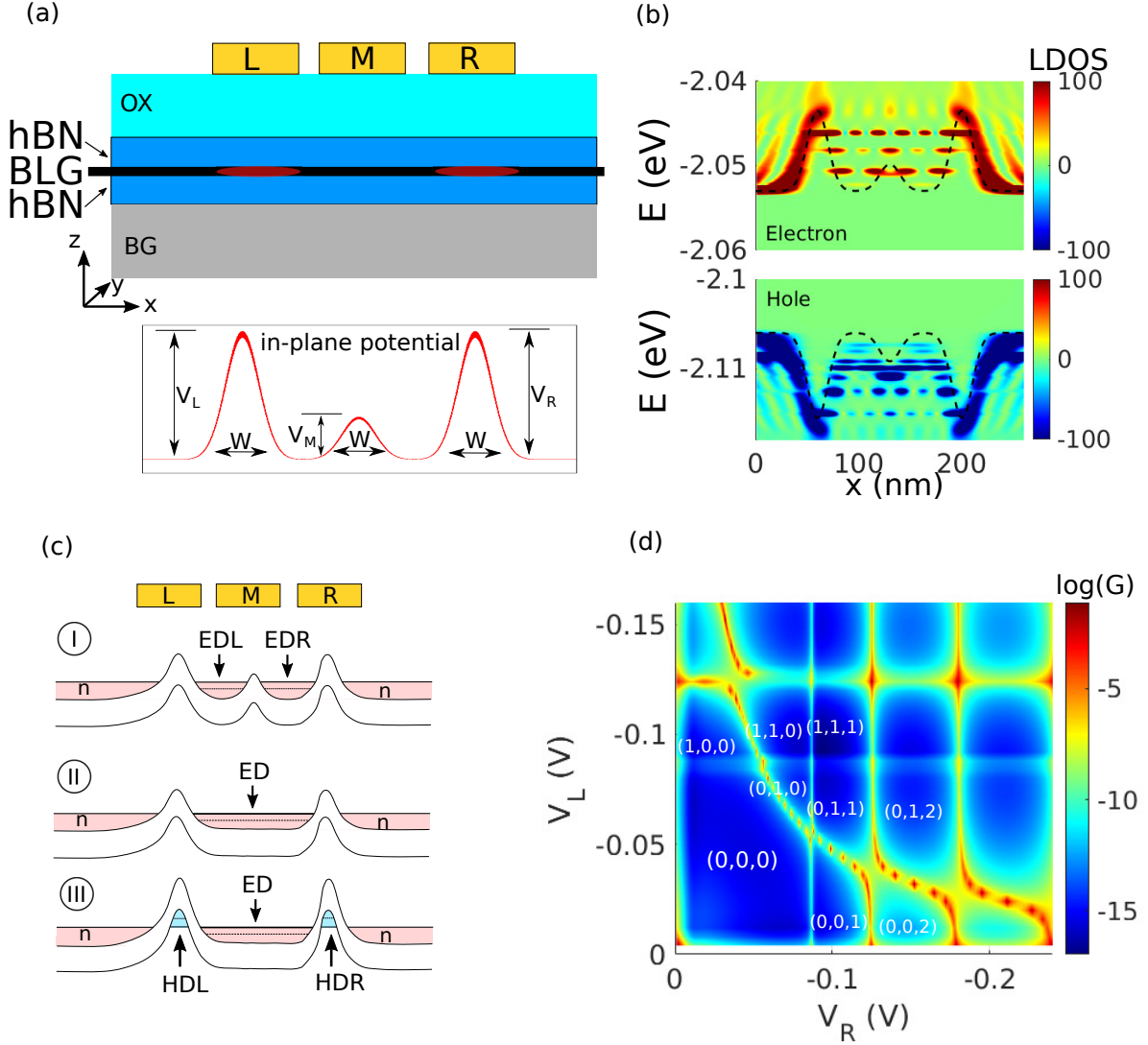


FIG. 3. (a) Simulation domain corresponding to a bilayer graphene (BLG) with a total length of 260 nm along the transport direction x and a width of 2.1 nm along y for a total of 42400 atoms, with the periodic boundary condition along y . A vertical electric field \vec{E} acts on the BLG and is applied through a back gate (BG) contact. The BLG is embedded between two hBN layers. The red regions under L and R indicate the position of the electrostatically confined quantum dots. The electrostatic potential is further controlled by three top gates labeled L, M, and R. They are separated from the BLG by a SiO_2 oxide and a hBN layer. The bottom inset shows a typical potential profile obtained by superposing Gaussian functions induced by each top electrode. (b) Local density-of-states of the electron and hole populations. Positive (negative) values refer to the top (bottom) layer, respectively. $\vec{E} = 0.5$ V/nm, $V_M = \pm 4$ mV, and $V_L = V_R = \pm 0.01$ V where + stands for hole while - for electron. The dashed lines represent the conduction and valence band edges. (c) Schematics of the band profile along the BLG sheet illustrating the formation of dots: (I) using the M gate, two n-doped islands form the desired electron dots (ED) with a tunneling barrier between them; (II) at $V_M = 0$, one large ED is formed; (III) at larger V_L and V_R , two additional hole dots (HD) are created under these gates. (d) Charge stability diagram: logarithmic conductance at a drain-to-source voltage $V_{DS}=0.1$ mV, Fermi level $E_F=-2.0525$ eV, $\vec{E} = 0.5$ V/nm, $V_M=0$ V and $k_B T=1$ μ eV as a function of the L and R gate voltages. The equilibrium charge number in HDL, ED and HDR are depicted as (N_0, N_1, N_2) .

plying different potentials to the bottom and top gates, the vertical electric field acting on the BLG can be precisely controlled. In addition, the potential landscape can be modified by tuning the top L, M, and R gates. The simulated device structure measures 260 nm along the transport direction, possesses zigzag edges, and is made

of 42400 atoms in total. The three top gates are 10 nm long and separated by 50 nm. Charge transport is solved with a quantum transport simulator [25] based on the *ab initio* Non-equilibrium Green's function (NEGF) formalism, as described in Appendix A. In this study, the potential profiles are approximated as Gaussian functions

that are plotted in the bottom inset of Fig. 3(a), Poisson's equation being not self-consistently solved due to the large computational burden associated with the consideration of thousands of gate voltage configurations.

Figure 3(b) shows that by applying $\vec{E} = 0.5$ V/nm and by properly adjusting the applied top gate voltages both electron and hole QDs can be generated in BLG, without spurious bandgap states and with a strong localization of the $|0\rangle$ and $|1\rangle$ states in the top and bottom graphene layer. The projected local density-of-states (LDOS) confirm that the qubit state defined in Fig. 2 is not altered by the confinement potential. By applying an appropriate bias to the top M gate (or plunger gate), a gradual transition from two QDs hosting electrons or holes to a single larger QD can be achieved, thus providing a way to tune the interdot tunnel coupling. This transition occurs between regime I and II in Fig. 3(c). The charge stability is demonstrated by the distinct resonances in the conductance map as a function of the gate voltages applied to the L and R electrodes, $V_{L,R}$, setting $V_M = 0$. $V_{L,R}$ creates two potential barriers that confine an electron dot (ED) in the middle and that tune its energy levels. Each time an energy level crosses the energy window defined by the Fermi energies of the source and drain contacts, a resonance peak can be seen in the conductance map (see Fig. 3(d)). In addition to creating n and p-type QDs in the central region, the electrostatic potential can also be shaped to form ambipolar QDs through the application of large enough L and R gate voltages, as highlighted by regime III in Fig. 3(c). The L/R gates closely control the energy levels in the hole dot (HDL/HDR) underneath it. Whenever the energy levels of the ED and HDL/HDR cross the energy window of interest, a crossing of two lines of maximum conductance can be observed in Fig. 3(d). We note that the observed high LDOS on the QD boundaries, which originated from the coupling to the continuum of states in the left and right contacts due to the NEGF open boundary condition, is expected to be reduced in a fully self-consistent Schrödinger-Poisson solution. However, we do not expect this to alter qualitatively our result because the conductance is limited by the electron states inside the quantum dot rather than in the boundaries.

In order to investigate the system scalability towards a highly integrable qubit platform, we also show the possibility of creating multiple qubits within one BLG device in Fig. 4. Since the electron and hole dots possess well-separated LDOS and charge densities localized in the top and bottom layers, they can be exploited for hosting $|1\rangle$ and $|0\rangle$ qubit states. It is worth noting that between the QDs, the Fermi energy lies inside the band gap, which leads to a finite region of zero charge density and a tunneling barrier. Figure 4(a) shows an n-p double-QD, while Fig. 4(b) presents a p-n-p triple-QD formed in the channel. A chain of QDs of $|1\rangle$ and $|0\rangle$ can be constructed via N top gates, thus promising easily scalable multi-qubit systems [8]. Contrary to the traditional charge qubits where two QDs are required to form a single

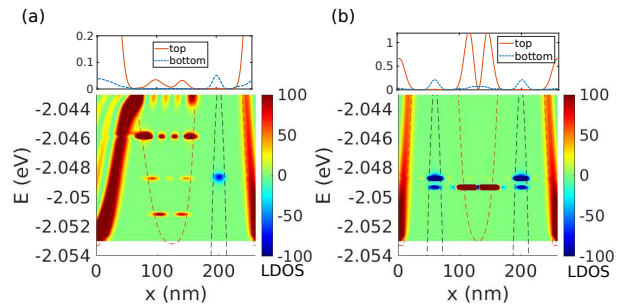


FIG. 4. Local density-of-states of the electron and hole population of BLG at a positive electric field of 0.5 V/nm. Positive (negative) values refer to the top (bottom) layer. (a) At gate voltages $V_M=0$ V, $V_R=-0.06$ V, and $V_L=-0.01$ V. (b) Same as (a), but at $V_L=-0.06$ V. The dashed lines represent the conduction and valence band edges. The corresponding charge density distributions in the top and bottom layers with $E_F=-2.048$ eV are plotted in the upper panels.

charge qubit [1, 26], a single vdW-bilayer QD is sufficient to form one qubit because the wave function in each dot is a quantum superposition of $|T\rangle$ and $|B\rangle$. Moreover, a single global bottom gate electrode reduces the number of gate electrodes, which greatly simplifies the geometrical complexity and increases the integration density of qubits. Coupling remote charge qubits has been experimentally demonstrated for graphene [27, 28] using microwave resonators, offering the possibility to entangle more-than-nearest-neighbor QDs. While the previous experiments show a viable path to implement a multi-qubit coupling scheme for the vdW-bilayer QDs, this remains a challenging task that will need detailed investigations in the future. They go far beyond the scope of our present work.

IV. TIME-DEPENDENT QUBIT MEASUREMENT

After demonstrating the qubit operation conditions and obtaining charge stability for multiple QDs, the procedure to read out the qubit state is now discussed. For time-dependent simulations, the qubit is modeled by a two-level Hamiltonian constructed from the DFT band-structure of 2D bilayers under different vertical electric fields

$$\hat{H}_Q(\vec{E}) = \epsilon_T(\vec{E}) |T\rangle \langle T| + \epsilon_B(\vec{E}) |B\rangle \langle B| - \frac{\Delta}{2} (|T\rangle \langle B| + |B\rangle \langle T|), \quad (2)$$

where $\epsilon_T(\vec{E})$ and $\epsilon_B(\vec{E})$ are the on-site energies of the top and bottom layer that depend linearly on \vec{E} , and Δ is the anti-crossing energy. These values are obtained by fitting the VBM and CBM energy levels for varying \vec{E} (see Fig. 2) to the eigenvalues of the quadratic Hamiltonian.

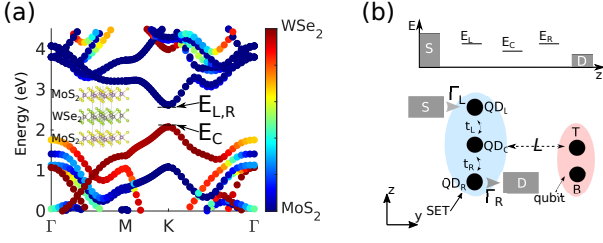


FIG. 5. (a) Electronic bandstructure of the trilayer vdW heterostructure MoS₂-WSe₂-MoS₂ for the SET measuring setup. The color of the states indicates the contribution from each individual MoS₂ and WSe₂ monolayer to the overall bandstructure. The inset represents the simulated vdW structure. (b) Conceptual representation of the whole system consisting of one vdW qubit (red circled) and a SET (blue circled) viewed from the y-z cross-section in Fig. 1(b). The relevant energy levels of QD_{L,C,R} are $E_{L,C,R}$, respectively. They are shown in the top sub-plot. The tunneling probabilities between the source, QD_{L,C,R} and the drain are Γ_L , $t_{L,R}$, and Γ_R , respectively. The SET is coupled through Coulomb interaction to the charge qubit located within a bilayer system at a distance L .

A SET formed by a linear array of three QDs capacitively coupled to the qubit is chosen for the measurement, as suggested in Ref. [29] and shown in Fig. 5(b). Such a configuration has an enhanced readout sensitivity as compared to the more common single QD SET. The designed SET is described by the following Hamiltonian operator,

$$\begin{aligned} \hat{H}_{\text{SET}} = & E_L |L\rangle \langle L| + E_R |R\rangle \langle R| + E_C |C\rangle \langle C| \\ & - t_L (|C\rangle \langle L| + |L\rangle \langle C|) \\ & - t_R (|C\rangle \langle R| + |R\rangle \langle C|) \\ & + \sum_{i,j=L,C,R} W_{i,j} |i,j\rangle \langle i,j|, \end{aligned} \quad (3)$$

where $|L\rangle$, $|R\rangle$, and $|C\rangle$ denote the single-electron states when the electron is located in QD_L, QD_R, and QD_C, respectively, and E_L , E_R , and E_C for the on-site energies; t_L and t_R indicate the tunneling probabilities between the QDs; $|L,R\rangle$, $|L,C\rangle$ and $|C,R\rangle$ are the two-electron states, while $W_{i,j}$ represents the Coulomb interaction between dots i and j . The electron density in the QD is assumed as a point charge. In this case the energies of the electrostatic interaction have the following values $W_{i,j} = 2\text{Ry} \times a_B/d_{i,j}$, where $d_{i,j}$ is the distance between the centers of the QDs i and j , $a_B = 0.52 \times 10^{-10}$ m is the Bohr radius, $\text{Ry} = 13.6$ eV is the Rydberg energy. This approximation works well for small-sized charge dots as the ones considered in this work [29]. The SET is only coupled to the qubit *via* the Coulomb interactions without any direct tunneling,

$$\hat{H}_{\text{Q-SET}} = \sum_{i=T,B;j=L,C,R} W_{i,j} |i,j\rangle \langle i,j|. \quad (4)$$

The time evolution of the density matrix operator $\hat{\rho}$ corresponding to the qubit-SET system was simulated by

solving the Lindblad equation [29, 30]. More details are given in Appendix B.

The optimal condition for the aforementioned triple-QD SET requires first that the energetic detunings between the external (QD_L, QD_R) and the central (QD_C) dots, $\delta_{L,R} = E_{L,R} - E_C$, are equivalent. Second, the electrostatic couplings W between the SET QDs and the qubit should be symmetric (asymmetric) for the electron in the top (bottom) layer, respectively. More explicitly, $W_{T,L} = W_{T,R}$ and $W_{B,L} \neq W_{B,R}$. We therefore propose a vdW heterostructure made of three 2D materials (MoS₂-WSe₂-MoS₂) as SET design, as illustrated in Fig. 1(b).

The projected bandstructure in Fig. 5(a) reveals that the CBM and VBM are located within one of the 2D layers. The degenerate CBM of the top and bottom MoS₂ layers define the energies of the external QDs L and R, and the VBM of WSe₂ realizes the central QD C. The direct bandgap at K in the Brillouin Zone corresponds to the symmetric detuning $\delta_{L,R}$. The vertical alignment of the top qubit layer with WSe₂ guarantees that the presence of an electron in this layer causes a symmetric renormalization of the energies in the SET. In contrast, an electron in the qubit bottom layer creates an imbalance of detunings and causes the current to cease. The triple-QD in the vdW heterostructure is formed electrically by a top gate electrode that induces a local confinement. To assess the impact of electron-phonon and electron-electron interactions on the measurement sensitivity of the coupled qubit and SET systems, we included the relaxation and dephasing rates γ_{rel} and γ_{dep} , accounting for those scattering processes, respectively. The corresponding collapse operator in the Lindblad equation is constructed as

$$\begin{aligned} \mathcal{C} = & \gamma_{\text{rel}} [\mathcal{D}(|C\rangle \langle L|) + \mathcal{D}(|C\rangle \langle R|)], \\ & + \gamma_{\text{dep}} [\mathcal{D}(|L\rangle \langle L| - |C\rangle \langle C|) + \mathcal{D}(|R\rangle \langle R| - |C\rangle \langle C|) \\ & + \mathcal{D}(|T\rangle \langle T| - |B\rangle \langle B|)], \end{aligned} \quad (5)$$

where $\mathcal{D}(\hat{O}) \equiv \hat{O}\hat{\rho}\hat{O}^\dagger - \frac{1}{2}[\hat{O}^\dagger\hat{O}, \hat{\rho}]$.

The qubit is initialized by the application of an external electric field into one of the two states $|0\rangle$ or $|1\rangle$. The system then evolves until it reaches a steady state at time $\sim 1/\Gamma_R$ where Γ_R is the escaping rate of the electrons to the drain (see Fig. 5(b)). The output current $I = 2\pi e\Gamma_R\rho_R/\hbar$ is proportional to the population in the SET $|R\rangle$ state ρ_R . In what follows, we set $\Gamma_R = \Gamma_L = 0.12$ THz in agreement with experimental studies [1]. To assess the measurement capabilities of the proposed SET we record its contrast C and conductance g_m during the qubit dynamics. Here, the contrast determines how well both qubit states can be distinguished. It is defined as

$$C = |I(1) - I(0)|/|I(1) + I(0)|, \quad (6)$$

where $I(0)$ and $I(1)$ denote the output current when measuring a qubit in the $|0\rangle$ and $|1\rangle$ states, respectively.

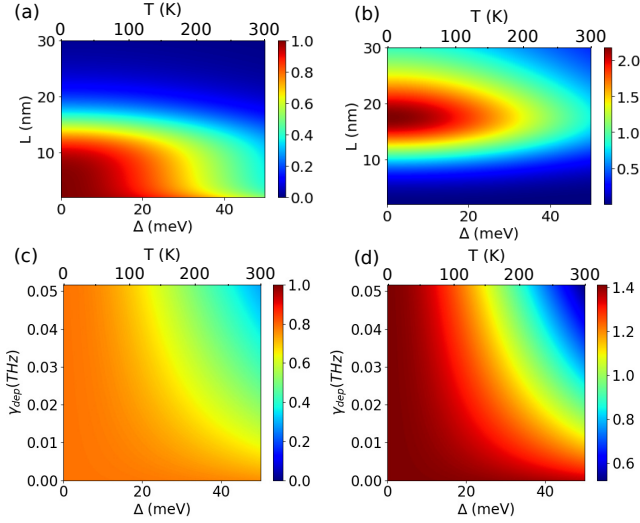


FIG. 6. (a) Contrast C of the designed SET as a function of the anti-crossing energy Δ and the distance L between the qubit and SET. (b) Same as (a), but for the differential conductance g_m in unit of (e^2/h) . (c) Contrast C and (d) differential conductance g_m as a function of Δ and of the dephasing rate γ_{dep} with $L=12.5$ nm. Δ relates to the thermodynamic temperature $T = \Delta/2k_B$ limiting qubit operation.

The differential conductance quantifying the SET current changes caused by variations of the qubit states is defined as [29]

$$g_m = Ce[I(1) + I(0)]/|W_{T,R} - W_{B,R}|. \quad (7)$$

The resulting contrast and differential conductance are plotted in Fig. 6 as a function of the qubit anti-crossing energy Δ and distance L between the qubit and SET with a characteristic time of $20/\Gamma_R$, including the aforementioned dissipative processes ($\gamma_{rel} = 0.05$ THz based on low-temperature transport measurement [31], while $\gamma_{dep} = 2\gamma_{rel}$ to account for the fact that dephasing happens faster than relaxation). The bottom left corner of Fig. 6(a) shows the limiting range of L (up to 13 nm) and Δ (up to 25 meV) to obtain high contrasts. Figure 6(b) also reports that g_m decreases as a function of Δ , but in a limited range of L values between 12 and 25 nm. Combining both sub-plots, it clearly appears that the optimal conditions for qubit measurement are $L=12.5$ nm and Δ between 0 and 25 meV. The maximum g_m value is higher than the experimental value reported in Ref. [32] using a different SET setup. A widely accepted idea is that a large Δ is desired between the qubit states, in order to make them energetically distinguishable from each other. A necessary, but insufficient condition is that Δ must be larger than two times the thermal energy ($2k_B T$) to suppress thermalization effects [33]. Therefore, a smaller Δ value necessarily entails a lower operation temperature of the qubit, as indicated by the upper abscissa in Fig. 6. Here, we show that a normally functional qubit also imposes an upper-limit on Δ , thus reducing the qubit design space.

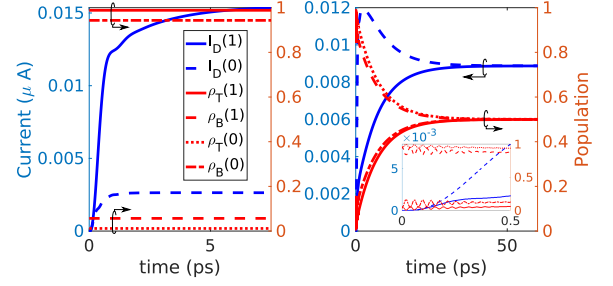


FIG. 7. (a) Time evolution of the drain current $I_D(0)$ and $I_D(1)$ flowing through a SET electrostatically coupled to a vdW qubit system with two logical states $|0\rangle$ and $|1\rangle$ and of the top layer ($\rho_T(0)$ and $\rho_T(1)$) and bottom layer ($\rho_B(0)$ and $\rho_B(1)$) population for the BLG system. (b) Same as (a), but for the $\text{ZrS}_2\text{-HfS}_2$ system. The inset shows the short-time evolution after the beginning of measurement.

To examine the intrinsic feasibility of vdW charge qubits, we study C and g_m as a function of the dephasing rate and anti-crossing energy in Fig. 6(c) and (d). The distance between the SET and qubit is fixed to 12.5 nm to ensure that both measurement quantities have high resolutions. It can be seen that the dephasing rate has a small impact on the degradation of C and g_m as long as Δ remains below 20 meV. However, when Δ exceeds 20 meV, g_m and C start to significantly decrease. This parameter region should therefore be avoided for the qubit design. This means that the anti-crossing energy is an intrinsically limiting factor, which suggests that the charge qubit should be defined with $\Delta \leq 20$ meV and the operating temperature lower than 120 K.

A typical time evolution of the drain current in this SET and the corresponding charge population in the qubit $|T\rangle$ (ρ_T) and $|B\rangle$ (ρ_B) states are presented in Fig. 7 for BLG and for $\text{ZrS}_2\text{-HfS}_2$. The BLG exhibits a much higher contrast of saturation current and almost no mixing. For $\text{ZrS}_2\text{-HfS}_2$, the strong Δ results in a fast qubit state mixing and consequently requires very rapid measurements within the picosecond time scale. By reducing the strength of Δ , for example by inserting an $h\text{BN}$ monolayer between the vdW bilayers, the qubit measurement quality can be recovered. These results underline

TABLE I. Summary of the material properties and qubit measurement results (C and g_m) for the BLG and $\text{ZrS}_2\text{-HfS}_2$ systems with $\vec{E} = -3$ V/nm, $\gamma_{dep} = 2\gamma_{rel} = 0.1$ THz. The Δ is the anti-crossing energy, whereas \vec{E}_{ac} denotes the electric field at the anti-crossing point when $t_{0,1} = b_{0,1}$.

	BLG	ZrS_2 (T)	HfS_2 (B)
Contrast [%]	71	26	
g_m [μS]	102	35.7	
Δ [meV]	0.02	174	
\vec{E}_{ac} [V/nm]	0	1.6	

the fact that high contrast qubit measurements are intrinsically not possible if the charge qubit is characterized by a large Δ . Table I summarizes the calculated qubit measurement results.

V. CONCLUSION AND DISCUSSION

In this work, we proposed a vdW charge qubit architecture based on 2D vdW materials. Our results indicate that the qubit states can be readily controlled by external electric fields. The two-level anti-crossing energy, which is related to the vdW interlayer coupling strength, can significantly vary between different material systems. Our quantum transport simulations suggest that quantum dots can be confined by electrically gating the vdW bilayer and that the coupling between neighboring quantum dots can be tuned by the gate potential. Furthermore, we also proposed a single-electron transistor (SET) design based on a trilayer vdW heterostructure and capacitively coupled to the quantum dot to measure the charge qubit state. Our time evolution simulations of the coupled qubit and SET systems reveal that the measurement sensitivity and contrast are affected by the intrinsic anti-crossing energy and by the dephasing processes in the vdW heterostructure. Our study identifies the optimal design parameter space to simultaneously achieve a low decoherence of the qubit states and enhanced measurement contrast and conductance.

In conclusion, our theory explains that upon the SET measurement the vdW-heterostructure qubit states rapidly degrade due to the large coupling intrinsically induced by anti-crossing energies higher than 20 meV. This phenomenon was not captured by previous theoretical studies. Among the systems we studied, bilayer graphene is the one maintaining the highest contrast between qubit states. Our findings show that 2D vdW structures can provide highly integrable all-electronic universal qubits. Our design of the coupled vdW qubit and SET system allows for an enhanced sensitivity of the charge qubit, thus paving the way for a scalable and CMOS-compatible quantum computing platform.

Appendix A: Ab initio quantum transport simulation

Following Ref. [20], a charge qubit can be defined in 2D bilayer materials through the superposition of a top ($|T\rangle$) and bottom ($|B\rangle$) orbital state, whose properties depend on a vertically applied electric field (\vec{E}). Since each local orbital occupies a different electrically-induced energy state, two distinct energy levels with different weights ($t(\vec{E})$ and $b(\vec{E})$) can be obtained (Fig. 1(a)). They are used as building blocks for the Bloch sphere and its $|0\rangle$ and $|1\rangle$ states, which form the two-level quantum system shown in Fig. 1(b). The latter is simulated at the *ab initio* level.

Through the QUANTUM ESPRESSO DFT package [34], the electronic structure of 2D bilayer materials is first obtained. The generalized gradient approximation of Perdew, Burke, and Ernzerhof (PBE) [35] is used as exchange and correlation functional, while the vdW interactions are taken into account with the DFT-D2 scheme of Grimme [36]. The plane-wave DFT Hamiltonian is then converted into a maximally-localised Wannier function (MLWF) basis with the Wannier90 code [37]. These results are scaled up [38] to construct the real-space device Hamiltonian and to perform realistic qubit device simulations based on the Non-equilibrium Green's Function (NEGF) formalism. The following equation is solved for the retarded Green's function \mathbf{G}^R ,

$$[E\mathbf{I} - \mathbf{H}_{\text{MLWF}} - \Sigma_{\text{S/D}}^R] \mathbf{G}^R = \mathbf{I}, \quad (\text{A1})$$

where E is the electron energy, \mathbf{I} the identity matrix, \mathbf{H}_{MLWF} the Wannier Hamiltonian matrix of the 2D bilayer graphene in the MLWF basis, and $\Sigma_{\text{S/D}}^R$ the retarded boundary self-energy accounting for the source and drain semi-infinite contacts. The observables of the system can be obtained from the retarded Green's function \mathbf{G}^R . The periodic boundary condition is imposed along the y direction as shown in Fig. 3(a). By including an electrostatically-induced confinement potential into \mathbf{H}_{MLWF} , a wide range of QD systems can be realized and their operation verified by inspecting the local density-of-states (LDOS). The electrical current of the device is calculated with the Landauer-Büttiker formula from the transmission probability $T(E)$ between two contacts [39, 40]

$$I = -\frac{e}{\hbar} \int \frac{dE}{2\pi} T(E) [f(E, E_{fL}) - f(E, E_{fR})], \quad (\text{A2})$$

with the elementary charge e . The two contacts are characterized by their Fermi distribution function f and Fermi levels E_{fL} and E_{fR} , whose difference depends on the applied source-to-drain voltage $E_{fL} - E_{fR} = eV_{DS}$. The conductance G is calculated as dI/dV_{DS} .

Appendix B: Evaluation of time-dependent Lindblad equation for qubit readout

The dynamics of the charge qubits is simulated with the QuTiP [21] package, which solves the Lindblad equation [29],

$$\begin{aligned} \frac{d\hat{\rho}}{dt} = & -i\hbar [\hat{H}_Q + \hat{H}_{\text{SET}} + \hat{H}_{\text{Q-SET}}, \hat{\rho}] \\ & + \mathcal{C} + \Gamma_R |vac_R\rangle \langle R| + \Gamma_L |L\rangle \langle vac_L|, \end{aligned} \quad (\text{B1})$$

where the qubit Hamiltonian (H_Q) is a two-level quantum system constructed from the electronic structure of a 2D bilayer material, while a three-level QD is used to represent the SET Hamiltonian (H_{SET}). The qubit and

SET parts are only electrostatically coupled through the electron-electron Coulomb interaction H_{Q-SET} , assuming no tunneling between them. The dissipative processes including relaxation and dephasing are described by the collapse operators \mathcal{C} in Eq. (5). The meaning and definition of each operator are given in Section IV. An arbitrary state as in Eq. (1) is evolved by integrating the set of ordinary differential equations that define Eq. (B1). The expectation value of the populations in the SET are recorded at each time step by means of the operators $\rho_L = |L\rangle\langle L|$, $\rho_R = |R\rangle\langle R|$, and $\rho_C = |C\rangle\langle C|$. The output at the last time step is used in Eqs. (6) and (7) to

asses the contrast and conductance of the proposed SET.

ACKNOWLEDGMENTS

This work was supported by the NCCR MARVEL and the NCCR SPIN of the Swiss National Science Foundation (SNSF), by SNSF under Grant No. 175479 (ABIME), by the Marie Skłodowska-Curie Grant No. 885893, and by a grant from the Swiss National Supercomputing Centre (CSCS) under Project s1119.

-
- [1] J. Gorman, D. G. Hasko, and D. A. Williams, Phys. Rev. Lett. **95**, 090502 (2005).
 - [2] R. Maurand, X. Jehl, D. Kotekar-Patil, A. Corna, H. Bohuslavskyi, R. Laviéville, L. Hutin, S. Barraud, M. Vinet, M. Sanquer, and S. De Franceschi, Nat. Commun. **7**, 13575 (2016).
 - [3] J. M. Gambetta, J. M. Chow, and M. Steffen, Npj Quantum Inf. **3**, 2 (2017).
 - [4] C. D. Bruzewicz, J. Chiaverini, R. McConnell, and J. M. Sage, Appl. Phys. Rev. **6**, 021314 (2019).
 - [5] R. Van Meter and C. Horsman, Commun. ACM **56**, 84–93 (2013).
 - [6] M. Eich, R. Pisoni, A. Pally, H. Overweg, A. Kurzmann, Y. Lee, P. Rickhaus, K. Watanabe, T. Taniguchi, K. Ensslin, and T. Ihn, Nano Letters **18**, 5042 (2018), publisher: American Chemical Society.
 - [7] A. Kurzmann, H. Overweg, M. Eich, A. Pally, P. Rickhaus, R. Pisoni, Y. Lee, K. Watanabe, T. Taniguchi, T. Ihn, and K. Ensslin, Nano Letters **19**, 5216 (2019), publisher: American Chemical Society.
 - [8] L. Banszerus, S. Möller, E. Icking, K. Watanabe, T. Taniguchi, C. Volk, and C. Stampfer, Nano Lett. **20**, 2005 (2020).
 - [9] K. S. Novoselov, A. K. Geim, S. V. Morozov, D. Jiang, M. I. Katsnelson, I. V. Grigorieva, S. V. Dubonos, and A. A. Firsov, Nature **438**, 197 (2005).
 - [10] C. Nayak, S. H. Simon, A. Stern, M. Freedman, and S. Das Sarma, Rev. Mod. Phys. **80**, 1083 (2008).
 - [11] Q. Xiaofeng, L. Junwei, F. Liang, and L. Ju, Science **346**, 1344 (2014).
 - [12] E. McCann and V. I. Fal’ko, Phys. Rev. Lett. **96**, 086805 (2006).
 - [13] E. McCann, D. S. Abergel, and V. I. Fal’ko, Solid State Communications **143**, 110 (2007), exploring graphene.
 - [14] M. Aoki and H. Amawashi, Solid State Communications **142**, 123 (2007).
 - [15] E. V. Castro, K. S. Novoselov, S. V. Morozov, N. M. R. Peres, J. M. B. L. dos Santos, J. Nilsson, F. Guinea, A. K. Geim, and A. H. C. Neto, Phys. Rev. Lett. **99**, 216802 (2007).
 - [16] J. B. Oostinga, H. B. Heersche, X. Liu, A. F. Morpurgo, and L. M. K. Vandersypen, Nature Materials **7**, 151 (2008).
 - [17] K. F. Mak, C. H. Lui, J. Shan, and T. F. Heinz, Phys. Rev. Lett. **102**, 256405 (2009).
 - [18] S. B. Kumar and J. Guo, Appl. Phys. Lett. **98**, 222101 (2011).
 - [19] D. S. Koda, F. Bechstedt, M. Marques, and L. K. Teles, Phys. Rev. B **97**, 165402 (2018).
 - [20] B. Lucatto, D. S. Koda, F. Bechstedt, M. Marques, and L. K. Teles, Phys. Rev. B **100**, 121406 (2019).
 - [21] J. R. Johansson, P. D. Nation, and F. Nori, Comput. Phys. Commun. **183**, 1760 (2012).
 - [22] S. Konschuh, M. Gmitra, D. Kochan, and J. Fabian, Phys. Rev. B **85**, 115423 (2012).
 - [23] L. Banszerus, S. Möller, C. Steiner, E. Icking, S. Trelenkamp, F. Lentz, K. Watanabe, T. Taniguchi, C. Volk, and C. Stampfer, Nature Communications **12**, 5250 (2021).
 - [24] G. Cao, H.-O. Li, T. Tu, L. Wang, C. Zhou, M. Xiao, G.-C. Guo, H.-W. Jiang, and G.-P. Guo, Nat. Commun. **4**, 1401 (2013).
 - [25] M. Luisier, Chem. Soc. Rev. **43**, 4357 (2014).
 - [26] D. Kim, D. R. Ward, C. B. Simmons, J. K. Gamble, R. Blume-Kohout, E. Nielsen, D. E. Savage, M. G. Lagally, M. Friesen, S. N. Coppersmith, and M. A. Eriksson, Nat. Nanotechnol. **10**, 243 (2015).
 - [27] G.-W. Deng, D. Wei, S.-X. Li, J. R. Johansson, W.-C. Kong, H.-O. Li, G. Cao, M. Xiao, G.-C. Guo, F. Nori, H.-W. Jiang, and G.-P. Guo, Nano Lett. **15**, 6620 (2015).
 - [28] G.-W. Deng, D. Wei, J. R. Johansson, M.-L. Zhang, S.-X. Li, H.-O. Li, G. Cao, M. Xiao, T. Tu, G.-C. Guo, H.-W. Jiang, F. Nori, and G.-P. Guo, Phys. Rev. Lett. **115**, 126804 (2015).
 - [29] A. V. Tsukanov, Phys. Rev. A **100**, 062305 (2019).
 - [30] D. Manzano, AIP Advances **10**, 025106 (2020).
 - [31] S. Engels, B. Terrés, A. Epping, T. Khodkov, K. Watanabe, T. Taniguchi, B. Beschoten, and C. Stampfer, Phys. Rev. Lett. **113**, 126801 (2014).
 - [32] C. Barthel, M. Kjærgaard, J. Medford, M. Stopa, C. M. Marcus, M. P. Hanson, and A. C. Gossard, Phys. Rev. B **81**, 161308 (2010).
 - [33] Y. Makhlin, G. Schön, and A. Shnirman, Rev. Mod. Phys. **73**, 357 (2001).
 - [34] P. Giannozzi *et al.*, J. Phys.: Condens. Matter **29**, 465901 (2017).
 - [35] J. P. Perdew, K. Burke, and M. Ernzerhof, Phys. Rev. Lett. **77**, 3865 (1996).
 - [36] S. Grimme, Journal of computational chemistry **27**, 1787 (2006).

- [37] G. Pizzi, V. Vitale, R. Arita, S. Blügel, F. Freimuth, G. Géranton, M. Gibertini, D. Gresch, C. Johnson, T. Koretsune, J. Ibañez-Azpiroz, H. Lee, J.-M. Lihm, D. Marchand, A. Marrazzo, Y. Mokrousov, J. I. Mustafa, Y. Nohara, Y. Nomura, L. Paulatto, S. Poncé, T. Ponweiser, J. Qiao, F. Thöle, S. S. Tsirkin, M. Wierzbowska, N. Marzari, D. Vanderbilt, I. Souza, A. A. Mostofi, and J. R. Yates, *Journal of Physics: Condensed Matter* **32**, 165902 (2020).
- [38] A. Szabó, A. Jain, M. Parzefall, L. Novotny, and M. Luisier, *Nano Letters* **19**, 3641 (2019), pMID: 31079463.
- [39] R. Landauer, *IBM Journal of Research and Development* **32**, 306 (1988).
- [40] M. Büttiker, *Phys. Rev. Lett.* **65**, 2901 (1990).